Corrosion Science 227 (2024) 111738

Contents lists available at ScienceDirect

Corrosion Science

journal homepage: www.elsevier.com/locate/corsci

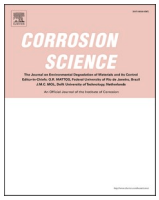

Comparative study on tribocorrosion behavior of hydrogenated/hydrogen-free amorphous carbon coated WC-based cermet in 3.5 wt% NaCl solution

Yingpeng Zhang [a,b], Hao Li [a], Li Cui [a], Wei Yang [a], Guanshui Ma [a], Rende Chen [a], Peng Guo [a,*], Peiling Ke [a,b], Aiying Wang [a,b,**]

[a] Key Laboratory of Marine Materials and Related Technologies, Zhejiang Key Laboratory of Marine Materials and Protective Technologies, Ningbo Institute of Materials Technology and Engineering, Chinese Academy of Sciences, Ningbo 315201, PR China
[b] Center of Materials Science and Optoelectronics Engineering, University of Chinese Academy of Sciences, Beijing 100049, PR China

ARTICLE INFO

Keywords:
DLC
WC cermet
Tribocorrosion
Structure evolution
Failure mechanism

ABSTRACT

In this work, the tribocorrosion performance of hydrogenated and hydrogen-free diamond-like carbon (DLC) coated thermal sprayed WC-based cermet/carbide were investigated comparatively. The results showed that, regardless of hydrogen containing, both coatings demonstrated the improvement of anti-tribocorrosion capability of WC-based cermet in 3.5 wt% NaCl solution, by suppressing the corrosion of Ni-based binder phases. Particularly, the hydrogenated DLC coating presented the better tribocorrosion resistance under low load due to the high hardness and excellent corrosion resistance, but it suffered from the catastrophic delamination and protective degradation at heavy load arisen from the high brittleness and large residual stress. In contrast, the hydrogen-free DLC duplex coating exhibited a low COF of ~0.06 under higher load (10 N) with long time friction (12 h), because of its gradually shearing characteristic. This work provides theoretical basis and design principles for DLC combinations with remarkable corrosion inhibition used in harsh marines.

1. Introduction

With the extensively increasing development of marine economy, high-level relevance to engineering equipment used in massive volume ocean environments has become more comprehensively important. In particular, to protect the mechanical components made of metals and steels during friction in harsh marine, thermal sprayed WC-based cermet/carbide coatings, as one of the promising functional layers with good mechanical properties and wear resistance, have been widely applied for the key tribological parts, such as oil/gas extraction valves as well as offshore pumps [1–5]. However, these WC-based coatings generally possessed coarse crystal structure and corrosion-prone binder phase, which make them apt to be worn during severe friction with heavy chloride induced corrosion for deep-sea applications [6–8]. Furthermore, the combination of pinhole/pore defects arisen from intrinsic growth of WC-based coatings easily caused the direct penetration of corrosive ions, leading to the catastrophic failure of coating with great risk of disasters [9,10]. Therefore, various attempts have been conducted to improve the tribocorrosion resistance of WC-based coatings without deterioration of the superior mechanical properties for marine infrastructures and key sliding components.

In recent years, hybrid utilization of physical vapor deposition (PVD) and thermal spray duplex coatings has been considered as the alternatively strongest strategy to solve the above-mentioned issues rather than each of the fabricated mono-coatings [11–14]. The advantages behind of this concept could be understood from two aspects. Firstly, the duplex coatings can overcome the "eggshell effect" of single PVD hard coatings on soft metallic substrates with heavy loads but poor loading durability. Secondly, the PVD top coating may act as functional layers and thereafter significantly improve the corrosion resistance and wear resistance as well as solid lubrication [15]. For example, Tang et al. [11] investigated the corrosion behavior of PVD CrN/high-velocity oxygen-fuel (HVOF) Cr_3C_2-NiCr duplex coatings in mixed salts. They found that, due to the sealing contribution from dense PVD-CrN top layer, the oxidation

* Corresponding author.
** Corresponding author at: Key Laboratory of Marine Materials and Related Technologies, Zhejiang Key Laboratory of Marine Materials and Protective Technologies, Ningbo Institute of Materials Technology and Engineering, Chinese Academy of Sciences, Ningbo 315201, PR China.
E-mail addresses: guopeng@nimte.ac.cn (P. Guo), aywang@nimte.ac.cn (A. Wang).

https://doi.org/10.1016/j.corsci.2023.111738
Received 19 October 2023; Received in revised form 18 November 2023; Accepted 30 November 2023
Available online 5 December 2023

of HVOF-coating was distinctly reduced by the combination of duplex coating, accompanying a much lowered thickness of formed oxides after 50 h thermal corrosion. Similarly, by facilitating the comparative CrN and diamond-like carbon (DLC) top layers by PVD techniques on HVOF deposited Fe_3Al-based coatings, Pougoum et al. [16] reported that both these PVD-CrN and PVD-DLC coatings presented the good wear resistance together with the low friction of coefficient (COF) comparing with that of pristine HVOF-coatings. On the basis of this conceptual approach to modifying tribological properties and corrosion durability, the evident prediction could be aimed by applying a combined PVD top layer over thermal sprayed coatings for the extended life-time of metallic engineering infrastructures in marine corrosive environments.

Among a vast amount of coatings deposited by various PVD techniques including magnetron sputtering and cathodic vacuum arc, nitrogen-based and carbon-based coatings are commonly used PVD protective candidates [17,18]. Especially, if one pays attention on both required low friction and high corrosion resistance, DLC coatings is of uttermost attractive as the most representative amorphous carbon-based protective materials, due to the high hardness, good self-lubrication and outstanding chemical inertness to severe acid-bases media [13,19–22]. In addition, the physiochemical properties of DLC coatings can be tailored by varying atomic carbon bonds and exclusive chemical dopants such as hydrogen, nitrogen and even metals. According to the typical ternary phase diagram [23], In general, DLC coatings could be categorized to hydrogenated and hydrogen-free amorphous carbon coatings. Comparing to hydrogen-free DLC coating (also well-known as graphite-like carbon, GLC), Zhang et al. [24] found that the hydrogenated DLC coatings demonstrated the superior wear resistance than GLC coating in an aqueous environment, in which the latter underwent much severer delamination and larger wear loss due to friction shearing. However, a contrast observation was that the hydrogenated DLC illustrated the extremely poor durability originated from the catastrophic delamination at interface of coating/substrate, while the hydrogen-free DLC was more favorable for the low friction and good wear resistance in an aqueous [25]. In this case, for the purpose of overcoming the largest challenges in reliability, safety and sustainability for key metallic components used in marine, hybrid manipulation of DLC coated HVOF layer would be extensively desirable to improve both tribological and corrosive properties under chloride solutions within a relatively long life-time and even a strong load-bearing capacity under deep-sea circumstances.

Previously, we have fabricated Cr/GLC multilayer coatings on 316 L stainless steels by multi-source DC magnetron sputtering (DCMS) and investigated the modulation periods effect on tribocorrosion behavior of coatings in artificial seawater [22]. The results showed that applying a hydrogen-free GLC top-layer with enhanced thickness could significantly improve the electrochemical corrosion capability to Cr/GLC coating. However, once the hydrostatic pressure was increased to 30 MPa, these Cr/GLC coatings severely suffered from the rapid degradation due to the localized pitting corrosion, which was accelerated by the growth defects and poor load-bearing tolerance [21]. In parallel, introduction of the Ti-TiCx/DLC gradient multilayer significantly benefited the long-term tribocorrosion properties of DLC coating on S32750 steel substrate, where a low COF value of 0.06 was obtained after sliding in 3.5 wt% NaCl solution more than 24 h under load of 20 N. However this coating was still worn out completely due to the poor fracture toughness [26]. From these perspectives, there is still a lack of fundamental understanding about which kind of DLC coating is the most suitable candidate to improve tribocorrosion resistance of mechanical components in harsh marine conditions. Therefore, in this work, we specialized the comparative study on the tribocorrosion behavior of duplex coatings composing of hydrogenated and hydrogen-free DLC coatings deposited on thermal sprayed WC-based coating, where the outmost DLC coating was particularly used as sealing and lubricant layer while WC-based cermet acted as the load-bearing transition layer. The failure mechanism for serviceability exposed chloride induced tribocorrosion was discussed in terms of the electrochemical behavior and microstructural evolution of coatings during various tests.

2. Experimental details

2.1. Coating preparation

Fig. 1a shows the synthesis procedure for duplex coatings containing of DLC top-layer next to HVOF sprayed WC-based cermet on Ti6Al4V substrates. Firstly, the WC-based cermet coating was prefabricated on the substrate by high-velocity oxygen-fuel (HVOF, JP8000, USA) spraying technology. A commercial WC-based powder (WC-20Cr_3C_2-7Ni, Chongyi Zhangyuan Tungsten Co., Ltd., China) with particle size distribution of 15–45 μm was used as the raw material for coating synthesis. The spraying step was set to 5 mm. The travelling speed and distance of the spray gun were 500 mm/s and 380 mm, respectively. More details about thermal spray process could be available elsewhere [27]. To suppress the growth defects such as pits and nodules in DLC top-layer during subsequent deposition, the as-deposited WC-based coating was polished, buffed, and ultrasonically cleaned to obtain an immaculate and a smooth surface. Then, hydrogenated DLC coatings were deposited by a linear ion source (LIS) with inputting C_2H_2 gas precursors, while hydrogen-free DLC coating was prepared by a DCMS feed with graphite source (purity of 99.99%) at working gas of Ar. Herein, C_2H_2 was selected as the carbonaceous gas rather than CH_4 due to the higher carbon-to-hydrogen ratio, which could allow the easier deposition of amorphous carbon coating with higher hardness related to hybridized sp^3 C-C bonds instead of C-H bonds. Prior to deposition, the base pressure of vacuum chamber was pumped to 3×10^{-3} Pa. The substrate was etched by Ar^+ ions for 30 min to remove the contaminants on substrate surface and improve the adhesion strength of coating. As for the deposition of hydrogenated DLC coating, the LIS source was operated at 0.2 A and 1200 V with inputting C_2H_2 flow rate of 38 sccm. The substrate was applied with a negative DC pulsed bias of − 100 V and the deposition time was controlled at 120 min. In case of hydrogen-free DLC, the graphite target was conducted at a DC current of 3.0 A and a power of 2.0 kW, in which the working gas of Ar was set at a flow rate of 60 sccm. The substrate bias voltage and the deposition time were maintained at − 200 V and 300 min, respectively. For the discussion simplicity, the WC-based coating prepared by HVOF was here labeled as the 'H' coating, while the duplex coatings with hydrogenated and hydrogen-free DLC coated on WC-based layer was assigned as 'HD' coating and 'HG' coating following, respectively. All the related DLC coatings was kept at a thickness about 1.7 μm by changing the deposition time for comparison.

2.2. Corrosion and tribocorrosion test

The instrumental apparatus and test procedure for the tribocorrosion experiment are shown in Fig. 1b-c. An electrochemical workstation (ModuLab XM ECS) was used to conduct electrochemical tests (ASTM G59–97) in 3.5 wt% NaCl solution, where a three-electrode electrochemical system was applied during measurement. Namely, the coated sample was set as the working electrode, a platinum plate acted as the counter electrode, and an Ag/AgCl electrode served as the reference electrode. The tribological behavior was investigated by a reciprocating tribometer (MFT5000, Rtec Instrument Technology Co., Ltd.), in which the Al_2O_3 ball with diameter of 6 mm was empolyed as the counterbody. The sliding distance and friction speed was kept at 4 mm and 20 mm/s, respectively. To compare the tribocorrosion properties of HD and HG duplex coatings under different loads and sliding times, the tests were particularly conducted at three characteristics: 5 N-1 h, 10 N-1 h and 10 N-12 h. As shown in Fig. 1c, the tribocorrosion procedure within an entire test was evolved two different stages. During stage 1, the open circuit potential (OCP) was monitored approximately within 1 h to ensure the stabilization of test sample before tribocorrosion measurement. Once the potential value of sample reached to stable state, the

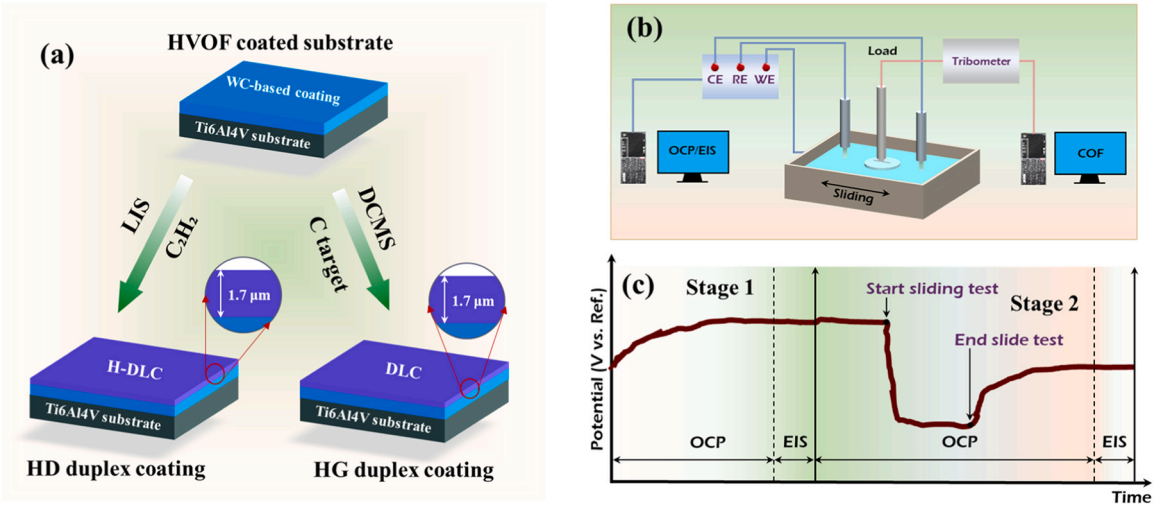

Fig. 1. Schematic diagram of (a) preparation procedure for duplex coating, (b) apparatus for tribocorrosion experiment, and (c) stage procedure conducted during tribocorrosion test.

corrosion resistance was started by electrochemical impedance spectroscopy (EIS). At stage 2, the sample was firstly allowed to soak naturally until the OCP was stabilized for the tribocorrosion test by reciprocating tribometer. After the ending of stage 2, the test was terminated until the OCP of the immersed sample was turned back stably, where the EIS was characterized to identify the corrosion resistance after tribocorrosion. During test period, all the data evolution including COF, EIS and OCP of coated samples were in-situ measured continually before, during and after tribocorrosion with real-time.

2.3. Characterization method

The surface morphology and elemental distribution of the samples were examined using a Quanta FEG 250 field emission scanning electron microscope (SEM, FEI, USA) equipped with an energy dispersive spectrometer (EDS). The chemical composition related to bond structure were comprehensively characterized by non-destructive Raman spectroscopy (Renishaw inVia-reflex, UK) and X-ray photoelectron spectroscopy (XPS, Kratos, AXIS SUPRA). After friction tests, the 3D images and the morphology of the wear track were observed by the UP-Lambda 3D optical profiler (Rtec, USA) and a Zeiss light microscope (Axio Imager 2). A scanning transmission electron microscope equipped with a focused ion beam (FIB-STEM, Auriga, Carl Zeiss, Germany) as well as electron energy loss spectroscopy (EELS) was employed to prepare the coated sample for TEM test and elucidate the microstructural features of coatings after tribocorrosion tests. The mechanical properties including hardness (H) and elastic modulus (E) of the duplex coatings were evaluated by a G200 nanoindentation tester (MTS, USA) in a continuous stiffness mode (CSM), with a Berkovich diamond indenter under a load depth to 500 nm. Each sample was tested 10 times to abate the measurement errors and the correspondent average value was taken as the output result. The adhesion strength between DLC top-layer coatings and WC-based cermet coatings were measured by the Revetest scratch test system (CSM) accompanied with an optical microscope and acoustic detector. The residual stress of the samples was tested using the stress tester, where the stress was calculated by comparing the change in curvature radius of the Si substrate before and after the coating deposition.

3. Results and discussions

3.1. Micromorphology and structure of deposited duplex coatings

Fig. 2 shows the cross-sectional SEM images of hydrogenated/hydrogen-free DLC as specified HD and HG top-layers, which was combined with the next HVOF-sprayed WC-based cermet layer on the Ti6Al4V substrate. The complete cross-sectional morphology containing each individual layer was also demonstrated in the Supplementary file of Fig. S1. As expected, the HD coating and the HG coating demonstrated the similar thickness about 1.71 μm and 1.74 μm as DLC top-layer

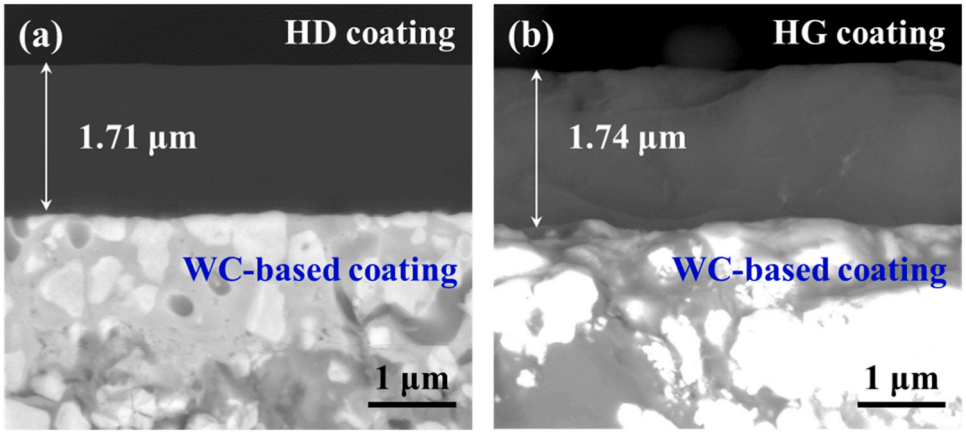

Fig. 2. Cross-sectional SEM images of (a) HD coating and (b) HG coating as top-layer deposited on WC-based cermet coating.

deposited on WC-based coating, respectively. Meanwhile, a dense growth and smooth surface without any obvious pores and cracks was visible for both DLC coatings regardless of hydrogen, in which a strongly bonded adhesion was illustrated as well for the duplex coatings.

Fig. 3a shows the Raman spectra of various DLC coatings deposited on WC-based cermet coating, where a typical amorphous carbon spectrum was distinctly observed for both HD and HG samples in the wavenumber range of 1000–1800 cm^{-1}. Since the Raman spectra of carbon materials could be deconvoluted into D peak centered around 1360 cm^{-1} and G peak located about 1560 cm^{-1} by Gaussian fitting method, the characteristics of carbon atomic bonds would be identified by the fitted G-peak position and the intensity ratio of D peak and G peak (I_D/I_G). Empirically, it is well-known that the higher G-peak position indicates the increase of graphitization in C-sp^2 bonds, while the lower I_D/I_G generally implies the smaller clusters size of ringed sp^2 phases [28]. After the deconvolution, an observation was that the I_D/I_G around 3.19 and G-peak position centered at 1552.15 cm^{-1} for HG sample was much larger than those of HD sample at 0.57 and 1537.54 cm^{-1}, respectively. It could thus be said that the HG coating contained much higher content of sp^2 bonds and larger sp^2 cluster size comparing with HD coating. Furthermore, the content of hydrogen in the hydrogenated amorphous carbon materials could be calculated using the following formula [29]:

$$H\left[at\%\right] = 21.7 + 16.6\log\left\{\frac{m}{I(G)}\left[\mu m\right]\right\} \quad (1)$$

where m represents the slope of the background line in the Raman spectrum, and $I(G)$ is the intensity length of the G peak (measured with unit of μm). Thereafter, the C-H content in the total C-sp^3 bond state was calculated to be around 22.15%, which was similar to the previous value of 20.6% detected by other elastic recoil detection analysis [30].

To further elucidate the chemical bonds in various DLC duplex coatings, Fig. 3c shows the representative C1s spectrum by XPS measurement for HD and HG coatings. Obviously, a broad peak assigned to amorphous carbon materials was visible on each of spectrum in range of binding energy at 281–291 eV. For each case, C 1 s peak mainly consisted of three fitting components, that could be the carbon hybridizations centered at 284.4 eV, 285.1 eV and 286.5 eV, corresponding to C═C (sp^2) bonded carbon, C-C/C-H (sp^3) bonded carbon and C-O/C═O relevant carbon. Noted that the sp^3 and sp^2 bonds represented the typical tetrahedral phase sp^3 and graphite phase sp^2 in amorphous carbon matrix, while the weak sate-like peak of C-O/C═O bonds was mostly ascribed to the residual oxygen adsorbed on sample surface exposed to air or relative pressure of vacuum chamber. As shown in Fig. 3d, the fitted content of C-O/C═O bonds in HD coating and HG coating was about 21.21% and 19.45%, respectively. However, the sp^3 content in HD coating was estimated around 60.52% (including part of 22.15% originated from C-H bonds), which was about two times larger than the value of 33.75% in HG coating. Correspondingly, the sp^2 bonds in HD coating (18.27%) was much lower than that in HG coating (46.79%). This observation proposed that the graphitization in hydrogen-free coating was much accelerated than that in hydrogenated DLC coating, which was strongly correlated to the carbonaceous gas of C_2H_2 used in HD deposition but pure graphite target source only applied for HG deposition without C_2H_2. Based on the traditional results [31, 32], the higher C-C sp^3 bond in amorphous carbon matrix would favor the superior mechanical properties including hardness and elastic modulus for DLC coating.

Considering the deviation in C-C and C-H sp^3 bonds were closely related to the mechanical properties of DLC coating, the STEM test accompanying with EELS analysis was further carried out. As shown in Fig. 4a-b, both HD and HG coatings displayed the contact and smooth morphologies together with a diffuse hallow patterns in the inserted

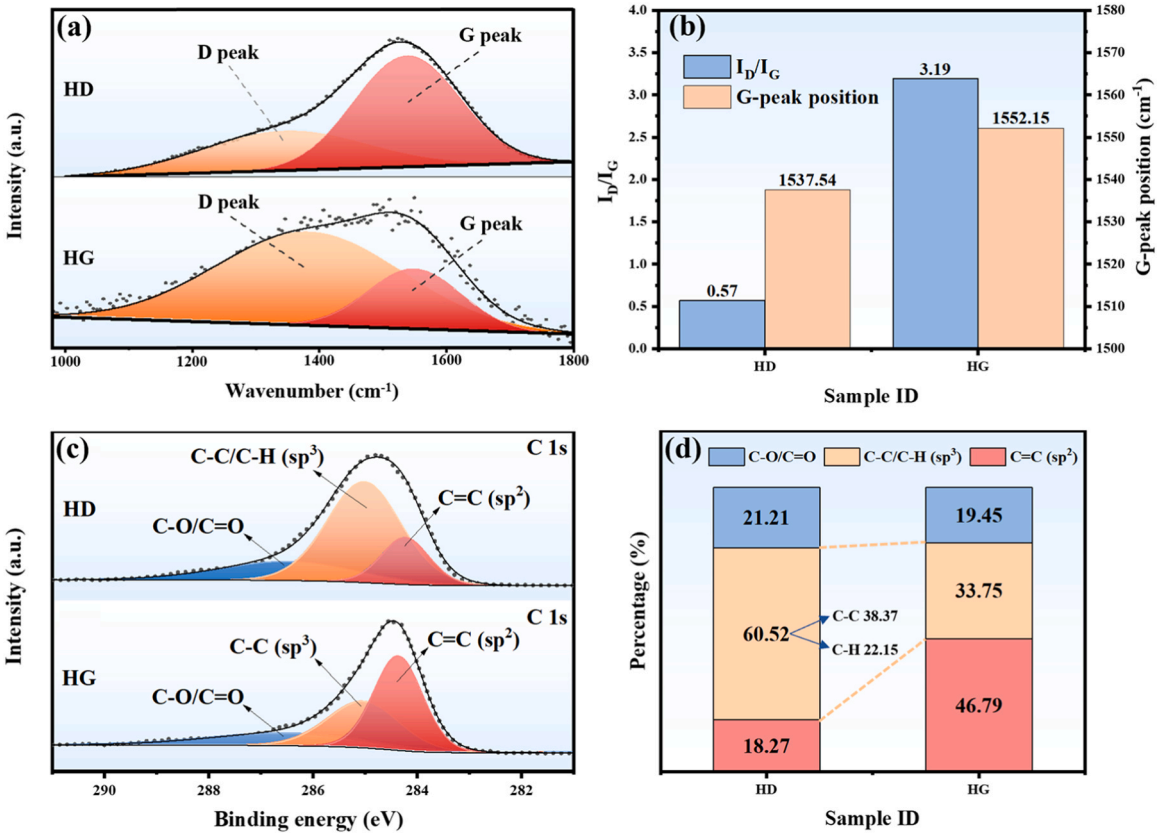

Fig. 3. (a) Raman spectra and (b) fitted G-peak position and I_D/I_G for various HD and HG duplex coatings; (c) XPS spectra and (d) fitted chemical bond composition of HD and HG coatings.

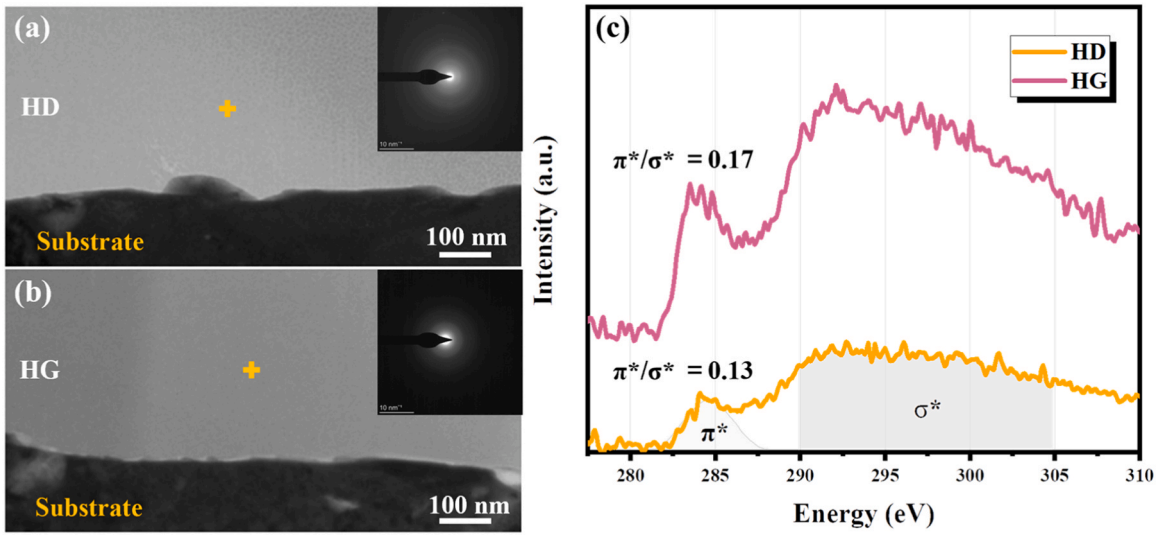

Fig. 4. Cross-sectional STEM image of the (a) HD coating and (b) HG coating deposited on HVOF-WC based cermet coating, and (c) corresponding carbon-K edge EELS result of the selected test area.

image of selected area electron diffraction (SAED), which was essentially the same as the traditionally pure DLC materials. Fig. 4c displays the carbon-K edge EELS spectra with a spatial resolution less than 1 nm derived from the marked area in Fig. 4a-b. By fitting each of the EELS curve [17], two peaks assigned to π * around 285 eV and σ * spanning a broad transition range of 290–305 eV could be used for the characterization of C═C sp^2 and C-C sp^3 hybridized bond in deposited DLC coating for comparison. It was observed that the intensity ratio of π * and σ * was 0.13 and 0.17 for HD coating and HG coating, respectively. This replied that the higher sp^2 content with stimulated graphitization in HG coating was achieved than that in HD coating, which agreed well with the XPS analysis.

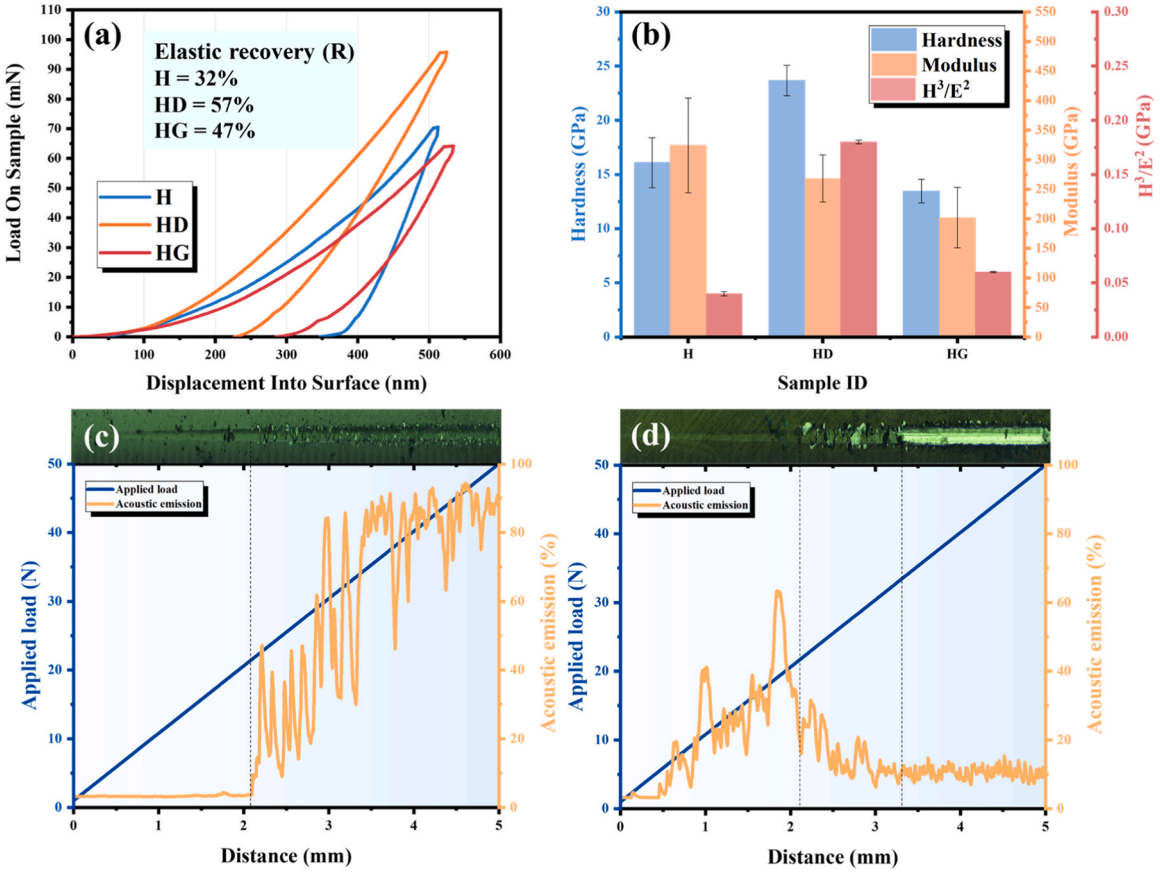

Fig. 5. (a) Nanoindentation load displacement curves of nanoindentation, (b) hardness and modulus values of the H, HD, and HG coatings, and (c) HD, (d) HG coating scratch track images and load vs acoustic signal-distance curves.

3.2. Mechanical properties of duplex coatings

Fig. 5a shows the in-situ load-displacement curves during nano-indentation tests for duplex DLC coatings on HVOF-WC cermet layer. No evident pop-in or pop-out event was visible from all three loading-unloading curves, demonstrating the lack of sudden contraction and expansion underneath the indenter regardless of amorphous carbon matrix. Noticeably, the elastic recovery of the HD coating was 57% as calculated by the formula [33], whereas it was only 32% and 47% for the H and HG coatings, respectively. Comparing to the average hardness value of 16.09 GPa for WC-based cermet coating, the duplex coating with HD layer and HG layer was about 23.66 GPa and 13.47 GPa, respectively, as shown in Fig. 5b. The slight decrease of hardness in HG duplex coating could be attributed to the dominated sp^2 bonds, as predicted from the XPS and EELS results. In other aspect, H^3/E^2 generally is a measure of plastic deformation capability of ceramic hard coating against a rigid contact. The larger H^3/E^2, the greater the contact yield compressive stress the coating can withstand, corresponding to the less likely plastic deformation and the better wear resistance with high toughness. Comparing with the H^3/E^2 value of 0.04 GPa for pure WC-based cermet coating, the H^3/E^2 value of HD and HG duplex coating was approximately around 0.18 GPa and 0.06 GPa, respectively. This observation indicated that the HD coating with the higher C-sp^3 bond possessed better wear resistance over HVOF-WC coatings and HG duplex coatings. However, another specific note was that the critical load, defined as the applied load at which the coating firstly began to delaminate accompanying with a distinct increase of acoustic signal, was similar at 21 N for both HD and HG duplex coatings. Base on this result, the good adhesion strength of DLC coatings regardless of hydrogen was generated on HVOF-WC cermet coating.

3.3. Tribocorrosion behavior of various coatings

Fig. 6 shows the tribocorrosion behavior for both HD and HG duplex coatings under load of 5 N in a short-term (1 h) test. Firstly, all the H, HD, and HG coatings displayed the superior anti-tribocorrosion capability than that of the pristine Ti6Al4V substrate (Fig. S2) under the 5 N-1 h test condition, suggesting the prolong tribocorrosion resistance of these coatings to a great extent. In contrast of the average high value of COF at 0.3 for WC-based coating without DLC top-layer, the lowered average COF around 0.06 was obtained for both HD and HG duplex coating, replying the hydrogenated/hydrogen-free DLC could significantly improve the lubricant properties of the WC-based coatings. Particularly, in case of HD coated WC-based duplex coating, the sliding curve was much stable with sliding time. The evolution of OCP values for all samples during tribocorrosion test was recorded in Fig. 6b. Prior to sliding, the initial OCP value of the HD coating was relatively higher compared to each of H coating and HG coating, suggesting the lowest corrosion tendency and higher electrochemical stability in HD case [34]. During the sliding, all the OCP values moved downwards suddenly. Meanwhile, unlike the H and HG coatings, the OCP in HD coating kept decreasing instead of entering a platform period immediately during an entire loading stage. After 1 h sliding, all the OCP turned back up sharply to a stabilized level.

According to the mixed potential theory (MPT), only a part of the working electrode (sample) could be mechanically loaded during tribocorrosion test [35,36]. Currently, the monitored potential was a mixed potential generated by the load-free (passivation) and load-in (depassivation) region's own potential. In the early stage of tribocorrosion, the wear track was gradually formed and expanded, corresponding to the increase of contact area. This explained the rapidly potential drop in all cases of H, HD, and HG coating at the beginning of sliding. Once the sliding process was plateaued (i.e., the end of the running-in period), the exposed contact area was remained relatively stable, which led to the equilibrium situation of OCP in H and HG coating. In contrast, the HD coating exhibited the persistent localized peeling during sliding, which suggested the continuous exposure of the chemically active substrate to the saline water (Fig. 6c-d). When the test was terminated, the fresh substrate surface beneath the contact area was immediately self-repaired (repassivation) to form a passivation film. Consequently, the OCP of all samples get back upwards rapidly. It was worth mentioning that the equilibrium potential of the HD coating remained the highest value at the end of tribocorrosion sliding, indicating the best corrosion resistance than both the H and HG samples. This phenomenon could be explained by the above-mentioned MPT, in which the potential of the WC-based layer exposed after sliding was low, but the potential outside the wear track was quite high. Thus, the total mixing potential of the HD coating still exhibited the highest value

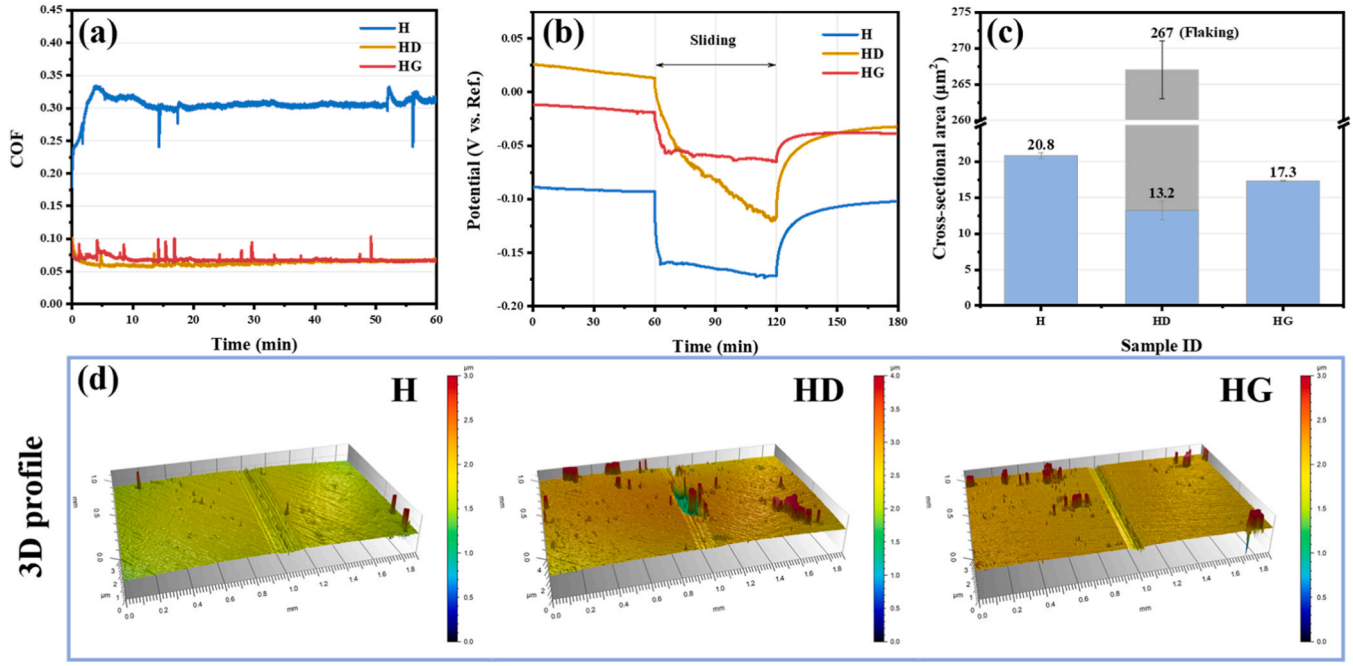

Fig. 6. (a) COF, (b) OCP, (c) cross-sectional area of wear track and (d) 3D profile of H, HD, and HG coatings under 5 N-1 h tribocorrosion test condition.

compared to the other samples.

In addition, the potential of H (↓0.009 V), HD (↓0.045 V) and HG (↓0.017 V) coatings decreased in various tendencies after tribocorrosion test. In particular, the corrosion resistance of the HD coating was degraded distinctly under 5 N-1 h tribocorrosion. Fig. 6c shows the estimated cross-sectional areas of the wear tracks for all three coatings. Compared to H coating at 20.8 μm^2 and HG coating at 17.3 μm^2, the HD coating possessed the lowest cross-sectional area in wear track around 13.2 μm^2. Although small pieces of localized delamination were visible in HD coating, the total wear loss along wear track was still lowest compared with the H and HG coatings.

Furthermore, to evaluate the tribocorrosion performance under a higher load, a normal load of 10 N was conducted in short time of 1 h for comparison. At the initial sliding stage, the COF values of HD and HG coatings almost overlapped around 0.06, which were far lower than that of H coating at 0.27 (Fig. 7a). However, the COF of HD coating started to rise steeply after 15 min test, indicating a severely catastrophic failure in HD sample. Different from the HD coating, the HG coating illustrated a quite stable COF around 0.06 without serious fluctuations. In this aspect, under heavy load of 10 N during tribocorrosion for 1 h, the HD duplex coating failed quickly after 15 min, while the HG coating exhibited a much longer service life for tribocorrosion application. Fig. 7b shows the OCP evolution of three coatings during tribocorrosion process. The H (−0.20 V), HD (−0.35 V), and HG (−0.07 V) coatings displayed the equilibrium potentials during sliding. Especially, a higher equilibrium potential was obtained in the HG duplex coating without any distinct exfoliation after sliding, but the quite worse degradation emerged in HD coated duplex coating due to the severely catastrophic delamination during sliding, occupying an accelerated low equilibrium potential arisen from the exposed fresh surface of WC-based cermet material.

As for the concern on the long-term tribocorrosion properties of HG coating, a representative test was specially conducted at 10 N-12 h condition for comparison. As shown in Fig. 8a, the HG duplex coating displayed the well stabilized friction characteristics with very low COF around 0.06 even extending tribocorrosion time to 12 h. The abrupt increase in COF curves for HG duplex coatings than that of HD sample during tribocorrosion sliding might be attributed to two aspects [37,38]. One was the continuous accumulation of wear debris generated with tribocorrosion sliding, where the larger particulates would cause the serious fluctuations. Another reason could be arisen from the stimulated shearing consumption within wear track in coating surface due to the relatively poor hardness of HG sample less than HD one, that enabled the fast removal of lubricant coating matrix and subsequently the severe friction with larger wear volume. Moreover, relevant evidence could also be visible from the sliding fluctuation of COF for HD coatings, which was similar to that of the COF evolution for HG sample (Figs. 6 and 7). Based on the inserted 3D profile and cross-sectional area taken from the wear track (inserts in Fig. 8), the interesting observation was that although the top-layer HG coating with thickness of 1.74 μm was most likely worn out, the excellent tribocorrosion resistance with low COF was demonstrated in the duplex coated substrate due to the accumulation of wear debris along wear track relevant to graphitized amorphous carbon particulates. Similar evidence could be indicated from the OCP result (Fig. 8b), in which a distinct fluctuation with steep dropping was visible during tribocorrosion process, replying the exposure and continuous plateau of the pristine WC-based coating.

3.4. Wear track evolution after tribocorrosion test

Fig. 9 shows the wear track characteristics for the samples of H, HD, and HG coatings. With same tribocorrosion test, increasing the applied load led to the increase of width wear track from 193.8 μm to 235.4 μm for the H coating (Fig. 9a and d), accompanying many obvious grooves distributed in the wear tracks. This essentially behaved the abrasive wear failure of thermal sprayed WC-based hard coatings when sliding with hard surface of Al_2O_3 counter-body, where the abrasive damage could be stimulated further by increasing load from 5 N to 10 N. However, once the HD coating was introduced on top of WC-based coating, the width of wear track was reduced significantly to 161.5 μm at 5 N-1 h (Fig. 9b), together with no more observation of abrasive grooves. The higher hardness (23.66 GPa) of HD duplex coating with graphitization transfer layer might be the key factor for such enhanced lubrications. Nevertheless, due to the existence of localized delamination of HD coating within wear track, it was notably that increasing the friction load to 10 N caused the exposure of underlying WC-based layer and the propagated wear failure with extended track width around 389.2 μm (Fig. 9e), where an obvious wear surface composing the centered worn out of HD coating and separated WC-based layer were visible. This

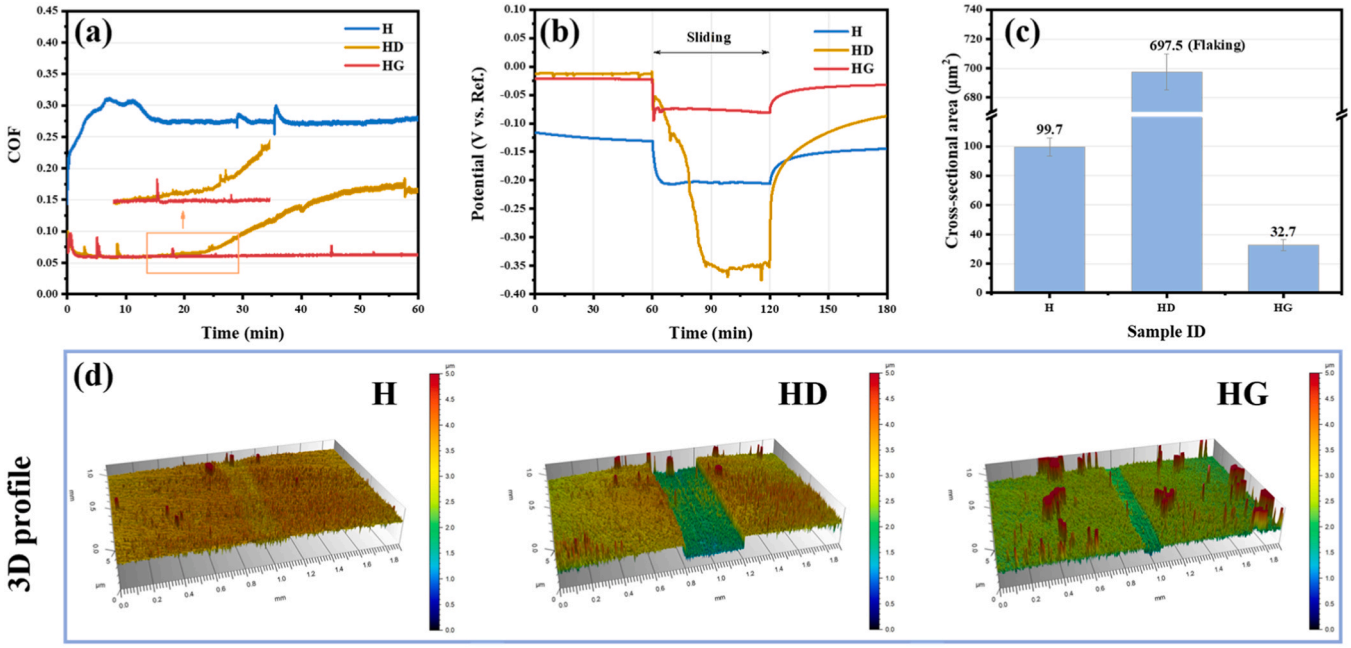

Fig. 7. (a) COF, (b) OCP, (c) cross-sectional area of wear track, and (d) 3D profile of H, HD, and HG coatings under 10 N-1 h tribocorrosion test condition.

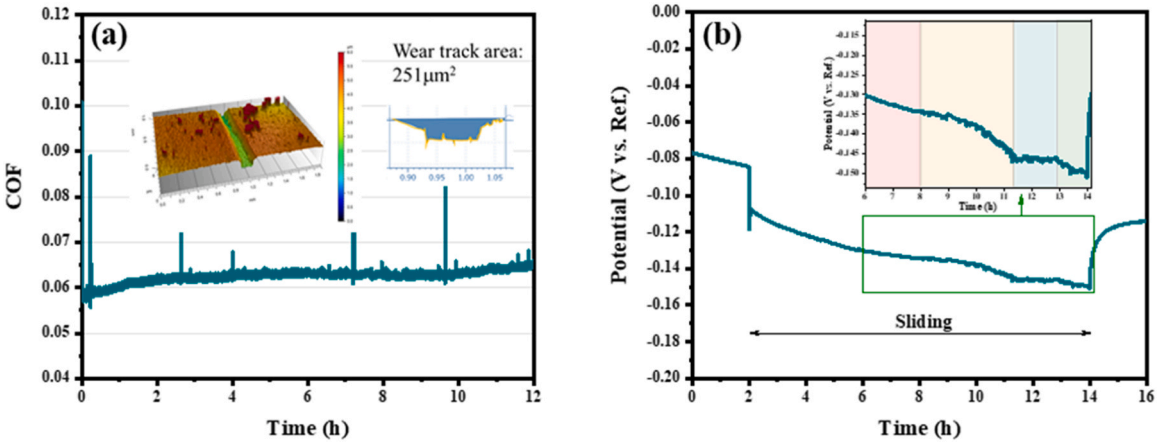

Fig. 8. (a) COF, 3D profile, cross-sectional area of wear track and (b) OCP of HG coating under 10 N-12 h tribocorrosion test condition.

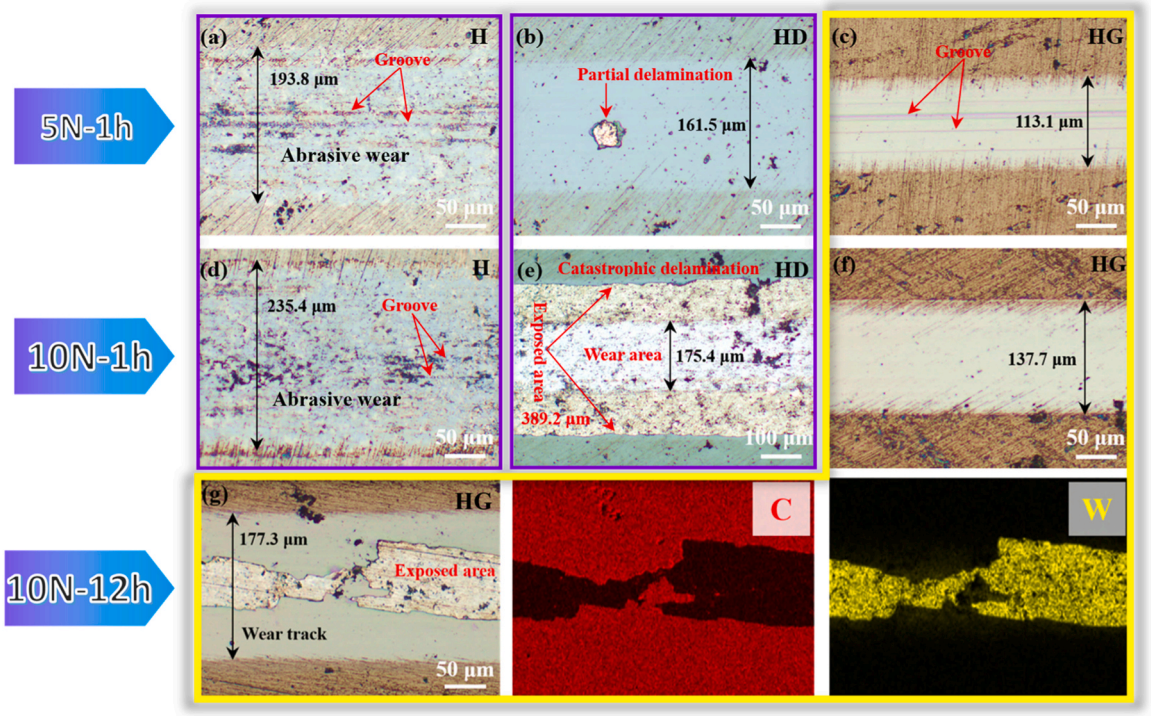

Fig. 9. Wear track morphologies of (a, d) H coating, (b, e) HD coating, (c, f) HG coating after tribocorrosion at 5 N-1 h and 10 N-1 h conditions, and (g) HG coating after tribocorrosion at 10 N-12 h condition.

discrepancy also agreed well with the OCP result showing continuous decline in mixing potential as well as the plateau stage at 10 N-1 h (Fig. 7).

Different from the HD duplex coating, the hydrogen-free DLC coated WC-based cermet illustrated a very excellent lubrication performance in chloride solution, showing a distinctly reduced wear track with width in range of 113.1–137.7 μm regardless of applied load (Fig. 9c and f). In addition, the HG duplex sample proposed a strong adhesion to next WC-based cermet since no any localized spallation or peeling off from top HG layer was induced by tribocorrosion. At 5 N-1 h, it was worth noting that the slight grooves along wear track emerged for HG coating, consisting with the mildly decrease and rapid plateau in OCP achievement (Fig. 6). With extended tribocorrosion test to 10 N-12 h, although the large pieces of delamination occurred in the centered HG outmost layer, the other residual amorphous hydrogen-free carbon distributed along wear edge acted well as the lubricants for the lower COF in HG duplex sample on Ti6Al4V substrate. Nevertheless, the elemental mapping implicated that the below WC-base ceramic layer was exposed gradually because of the intensive removal of relatively soft graphitic HG layer during sliding, where this conclusion could be also evidenced from the changes in OCP analysis (Fig. 8).

To further address the wear behavior of HG duplex coating at 10 N-12 h, we conducted the combined FIB-STEM measurement after tribocorrosion test. As shown in Fig. 10, the residual region was mainly composed of the dense and smooth hydrogen-free amorphous carbon structure except for the very faint cracks (labeled by arrow). However, once the heavy load was applied, these cracks might be extended or propagated, which thereafter induced the easy penetration of corrosive chloride medium to interfaces between HG/WC layers or even WC/substrate. In case of the exposure time enough long, the preferential corrosion pits happed in the Ni-based binder phases of coated WC cermet layer. From this, the degradation of tribocorrosion resistance for

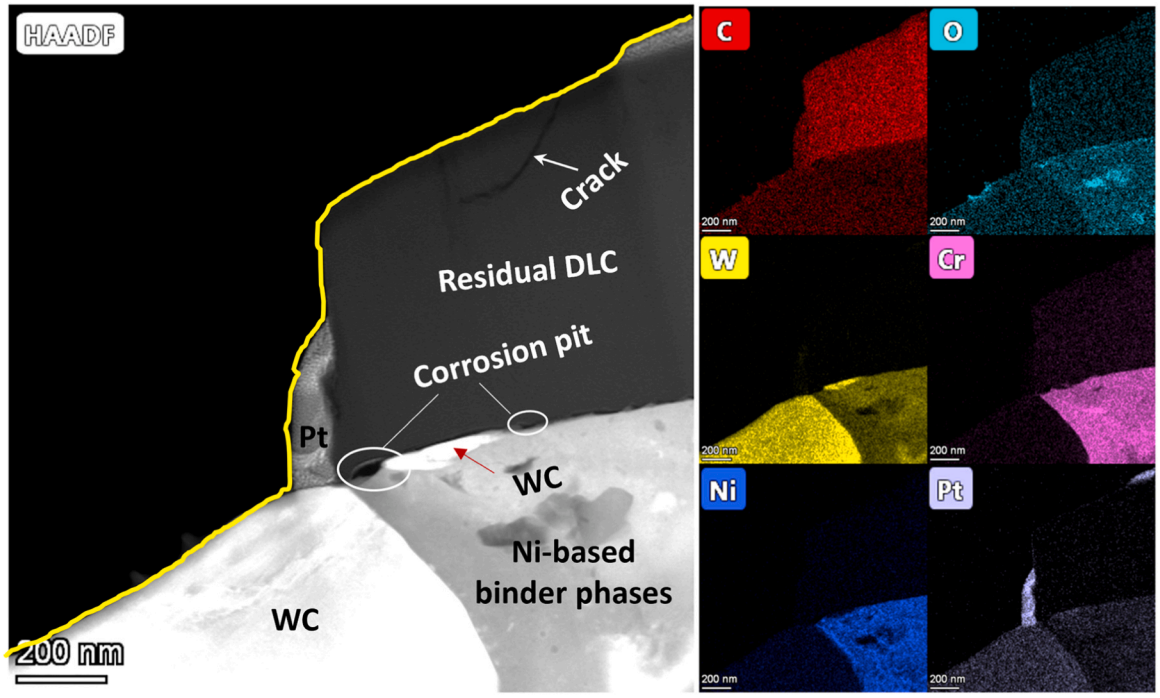

Fig. 10. The FIB-STEM measurement on structural characteristics of the wear track for HG coating at 10 N-12 h after tribocorrosion test.

the HG duplex coatings was observed comparatively.

3.5. Corrosion properties before and after tribocorrosion test

The EIS evolution of the H, HD, and HG coatings was monitored by in-situ electrochemical techniques. The EIS results of all samples under different conditions (initial state, 5 N-1 h and 10 N-1 h) are shown in Fig. 11.

From the Nyquist plots of H, HD, and HG coatings in Fig. 11a_1, b_1, and c_1, the capacitive arc radius decreased in all samples after sliding, besides, the Bode impedance plots (Fig. 11a_2-c_2) revealed that the impedance modulus ($|Z|_{0.01\ Hz}$) decreased with varying degrees for all samples, indicating that the corrosion resistance of the three coatings deteriorated after tribocorrosion. At the same time, the Bode phase plots (Fig. 11a_3-c_3) demonstrated that the phase angle of the post-tribocorrosion coatings was lower in the medium to the low-frequency region (10^2-10^{-2} Hz) compared to the pre-tribocorrosion coatings. In addition, compared to H and HG coatings, the phase angle dropped at the high-frequency region (10^5-10^4 Hz) was more pronounced for HD coating, which showed a positive correlation with the sliding load. This indicated that the high loads severely weakened the barrier effect of the HD coating to corrosion solution. Furthermore, to quantitatively study and compare the changes in corrosion resistance of H, HD, and HG coatings during the tribocorrosion tests, the EIS results of all samples were fitted using the ZView software. The equivalent circuit model used for the EIS fitting is shown in Fig. 12, where R_s, R_p, R_{ct}, CPE_{dl}, and CPE_c. R_s, R_p, and R_{ct} represent the solution resistance, pore resistance in the coating, and charge transfer resistance of the electric double layer at the coating/substrate interface, respectively. Due to the rough or porous surface of the sample, a CPE (constant phase element) is used in the model instead of C (capacitance) to compensate for the heterogeneity in the system. Thus, CPE_{dl} and CPE_c denote the capacitive characteristics of the electric double layer at the coating/substrate interface and the entire coating system, respectively. The impedance mode values of H, HD, and HG coatings as well as the EIS fitting results are presented in Fig. 12 and Table 1.

The initial R_p of the H, HD, and HG coatings were 9.42×10^2 Ω·cm^2, 9.84×10^4 Ω·cm^2 and 1.22×10^4 Ω·cm^2, respectively. Both hydrogenated and hydrogen-free DLC could significantly improve corrosion resistance of the H coating, and the HD had obviously better corrosion resistance than the HG. The initial R_{ct} and $|Z|_{0.01\ Hz}$ of HD coating were 7.11×10^{12} Ω·cm^2 and 5.44×10^5 Ω·cm^2 respectively, which were much higher than that of the HG coating (4.48×10^5 Ω·cm^2, 6.22×10^4 Ω·cm^2). It further proved that the HD coating provided superior corrosion resistance than the HG coating. It was worth noticing that R_p, R_{ct} and $|Z|_{0.01\ Hz}$ values of both HD and HG coatings decreased significantly with increasing sliding load. Even so, after tribocorrosion test at 10 N-1 h, R_p, R_{ct} and $|Z|_{0.01\ Hz}$ of the HD coating (6.52×10^4 Ω·cm^2, 2.52×10^8 Ω·cm^2, 2.42×10^5 Ω·cm^2) were still considerably higher than that of the HG coating (1.53×10^3 Ω·cm^2, 1.35×10^5 Ω·cm^2, 2.93×10^4 Ω·cm^2). This result suggested that the electrochemical activity of the HD coating was lower than the HG coating both before and after tribocorrosion test.

The impedance response of CPE can be obtained by the following equation [39]:

$$Z_{CPE} = \frac{1}{Q(j\omega)^{\alpha}} \tag{2}$$

where Q and α represent the two parameters of CPE, CPE-T, and CPE-P, respectively. When $\alpha = 0$, Q represents the ideal resistor; when $\alpha = 1$, Q signifies the ideal capacitor, and only then the Q has the capacitance unit (F·cm^{-2}). In addition, when $0 < \alpha < 1$, the α value can be considered as the extent to which Q approaches the ideal capacitance [40]. Here, both CPE_c-T and CPE_{dl}-T (F·cm^{-2}·s^{n-1}) did not have capacitance units. To obtain an accurate capacitance of the coatings before and after tribocorrosion, the effective capacitance (C_{eff}) of the HD and HG coatings was calculated by the following equation [41]:

$$C_{eff} = Q^{1/\alpha}\left(\frac{R_e R_t}{R_e + R_t}\right)^{(1-\alpha)/\alpha} \tag{3}$$

where R_e represents the ohmic resistance in the whole system. R_t, Q, and α can be regarded as integral properties, representing the capacitive circuit generated by R_t. The effective capacitance of the HD and HG coatings for the whole system (C_{eff}-C) and the electric double layer (C_{eff}-dl) is summarized in Fig. 13. It was found that sliding (both 5 N-1 h and

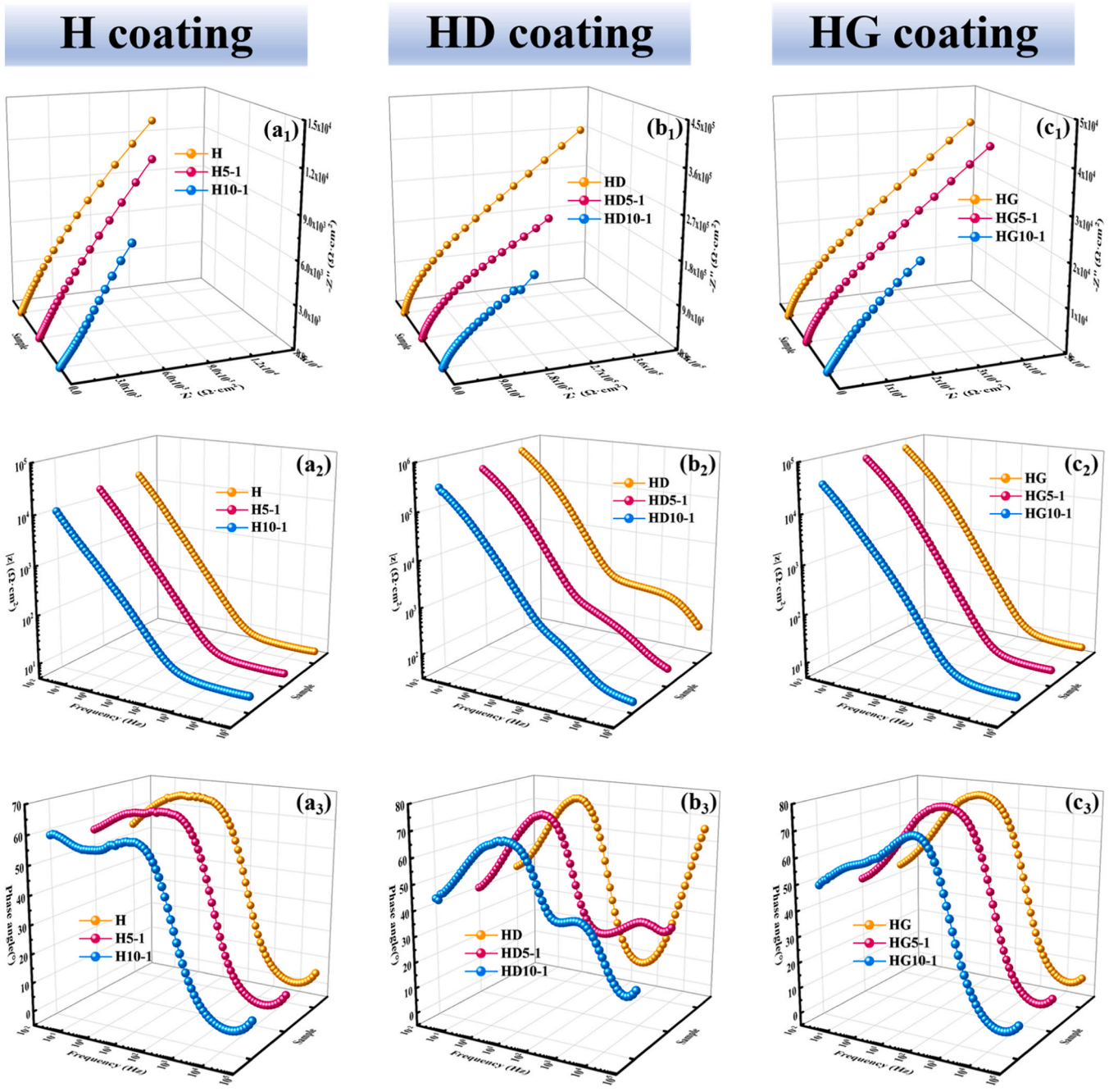

Fig. 11. EIS results of (a_1-a_3) H coating, (b_1-b_3) HD coating, and (c_1-c_3) HG coating before and after tribocorrosion at 5 N-1 h and 10 N-1 h.

10 N-1 h conditions) had a little influence on the capacitance of the two coatings, whether C_{eff}-C (Fig. 13a) or C_{eff}-dl (Fig. 13b). Capacitance reflects the amount of charge stored in a circuit, and the smaller the capacitance, the less charge accumulation [39]. So the sliding process seemed to have no significant effect on the amount of charge accumulation for both coatings. It may be due to the relatively small proportion of the contact area compared to the sample area. However, the C_{eff}-C and C_{eff}-dl of the HD coating were about one order of magnitude lower than that of the HG coating before and after tribocorrosion test, respectively. Therefore, the charge accumulation of the HD coating was remarkably lower than the HG coating, which implied that the HD coating always had lower electrochemical reactivity.

In short, the electrochemical results indicated that hydrogenated DLC was highly effective in enhancing the corrosion resistance of the WC-based cermet coating compared to hydrogen-free DLC. In addition, the corrosion resistance of both the HD and HG coatings showed a downward trend after tribocorrosion test, especially for HD coating under a high-load condition. Nevertheless, the electrochemical activity of the HD coating was greatly lower than the HG coating both before and after tribocorrosion test, exhibiting a superior corrosion resistance. The above observations were further confirmed by the potentiodynamic polarization (PDP) tests conducted before and after tribocorrosion (Fig. S3), where the HD duplex coating evidenced the best corrosion resistance than both of pristine H and HG coated samples. Specifically, the corrosion current density (*Icorr*) and potential (*Ecorr*) of HD coating were approximately (3.97×10^{-8} A/cm^2, 5.62×10^{-8} A/cm^2) and (-0.156 V, -0.127 V) before and after sliding test in 3.5 wt% NaCl solution, respectively. Moreover, the slight changes caused by tribocorrosion indicated the excellent stabilization and long durability of HD and HG coatings as protective layers.

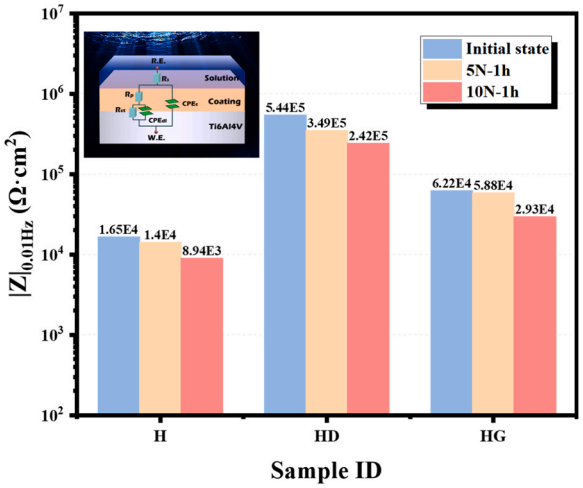

Fig. 12. The impedance modulus values ($|Z|_{0.01\ Hz}$) for H, HD, and HG coatings before and after tribocorrosion under different loads (The inserted image is the equivalent circuit model used for EIS fitting.).

According to above-mentioned analysis, the role of testing time and load on their tribocorrosion properties could be as follows. The HD coating had the highest hardness and H^3/E^2, implying its best wear resistance. Besides, the HD coating also provided the best corrosion resistance. Under lower load of 5 N, the HD coating only underwent few local delaminations and still kept its outstanding anti-tribocorrosion performance; Under higher load up to 10 N, HD coating suffered the catastrophic "avalanche" type delamination and exhibited the quick failure, two main reasons should be considered here. First, the highest hardness and sp^3 content in HD coating suggested its high brittleness, in addition, the residual stresses of this hydrogenated DLC tested was up to 1.5 GPa (Fig. S4), which can also increase significantly with the rise of relative humidity [42,43]. Both high brittleness and large internal stress of this hydrogenated DLC may cause great mismatch of the film-substrate and break of the top coating [44], especially under high load and large deformation conditions. Next, this catastrophic delamination would expose the bottom WC-based cermet, and the following corrosion pits will accelerate coating peeling. While, the HG coating had the lower hardness, less sp^3 content and lower water molecule sensitivity on its residual stress [22], therefore no peeling was observed both under 5 N-1 h and 10 N-1 h tribocorrosion tests. The gradual removal of the HG coating could explain its relatively worse performance under 5 N and better protection capability under 10 N.

It should be also noted that, under 5 N-1 h tribocorrosion condition, the cross-sectional area of the wear track in the unflaked region of the HD coating (13.2 μm^2) was smaller than that of the HG coating (17.3 μm^2) (Fig. 6). In addition, the HD coating showed the best anti-tribocorrosion performance compared to the H and HG coatings at 3 N-1 h condition, and the HD coating did not flake during the sliding process (Fig. S5). These phenomena suggested that once the DLC could avoid the catastrophic delamination, the hydrogenated DLC would endow the WC-based cermet with better tribocorrosion resistance than the hydrogen-free DLC. The schematic of the tribocorrosion process of the HD and HG coatings are illustrated in Fig. 14.

4. Conclusion

In summary, the hydrogenated and hydrogen-free DLC coatings were prepared on thermally sprayed WC-based cermet by LIS and DCMS techniques, respectively. The tribocorrosion properties of duplex coatings were comparatively investigated by potentiostatic and potentiodynamic measurements. The results showed that both hydrogenated and hydrogen-free DLC could dramatically enhance the protection capability of WC-based cermet in chlorine corrosive solution, by suppressing the corrosion of Ni-based binder phases. Specifically, the hydrogenated DLC modified WC-based cermet exhibited the higher hardness and stronger interface adhesion, which enabled them the superior tribocorrosion inhibition properties at low friction force (5 N). Due to the intrinsic large

Table 1
EIS fitting results of the H, HD, and HG coatings.

Sample	H coating			HD coating			HG coating		
Results	Initial state	5 N-1 h	10 N-1 h	Initial state	5 N-1 h	10 N-1 h	Initial state	5 N-1 h	10 N-1 h
Rs ($\Omega \cdot cm^2$)	9.17	9.39	10.68	9.89	11.56	10.28	11.06	10.95	10.41
CPEc-P	0.83	0.825	0.774	0.929	0.883	0.81	0.884	0.88	0.869
CPEc-T ($F \cdot cm^{-2} \cdot s^{n-1}$)	2.31×10^{-4}	2.53×10^{-4}	3.52×10^{-4}	5.23×10^{-6}	8.21×10^{-6}	1.43×10^{-5}	4.62×10^{-5}	4.74×10^{-5}	7.16×10^{-5}
Rp ($\Omega \cdot cm^2$)	9.42×10^{2}	4.01×10^{2}	3.47×10^{2}	9.84×10^{4}	9.03×10^{4}	6.52×10^{4}	1.22×10^{4}	1.17×10^{4}	1.53×10^{3}
CPEdl-P	0.58	0.556	0.601	0.424	0.422	0.371	0.489	0.468	0.581
CPEdl-T ($F \cdot cm^{-2} \cdot s^{n-1}$)	1.74×10^{-4}	2.46×10^{-4}	4.13×10^{-4}	5.78×10^{-6}	8.72×10^{-6}	1.32×10^{-5}	5.27×10^{-5}	5.58×10^{-5}	1.26×10^{-4}
Rct ($\Omega \cdot cm^2$)	1.98×10^{5}	1.79×10^{5}	9.23×10^{4}	7.11×10^{12}	4.73×10^{10}	2.52×10^{8}	4.48×10^{5}	4.14×10^{5}	1.35×10^{5}

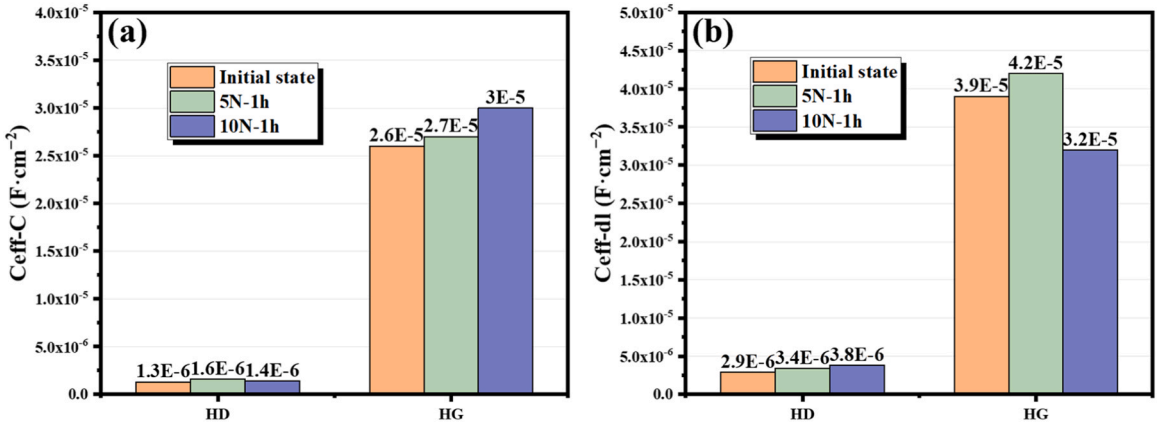

Fig. 13. Calculated effective capacitances of HD and HG coatings: (a) C_{eff}-C and (b) C_{eff}-dl.

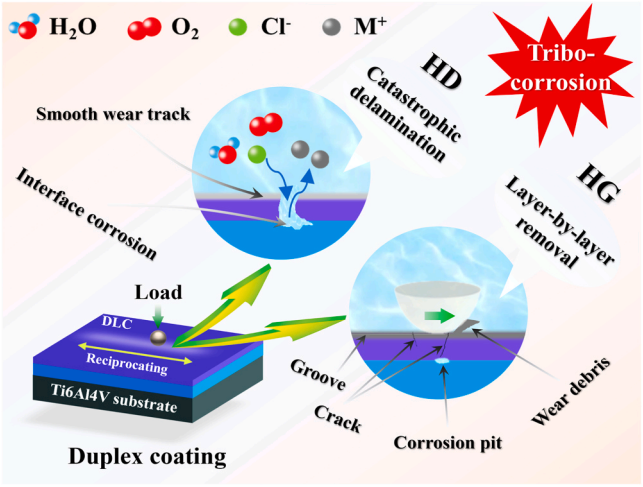

Fig. 14. The schematic of the tribocorrosion process of the HD and HG coatings.

residual stress and brittleness, such hydrogenated duplex coatings were easily worn out because of the catastrophic delamination at heavy load (10 N). In contrast, for the case of hydrogen-free DLC duplex coating, the gradually removal characteristic during friction shearing caused the relatively worse capability to tolerate the tribocorrosion under lower load, but the opposite excellent protection could be obtained at heavy load due to the outstanding toughness. As a result, it could be concluded that the WC-based cermet coated with duplex hydrogenated DLC was preferred for the tribocorrosion resistance served at lower load in chloride solutions, while the hydrogen-free DLC duplex candidate would be the best choice for heavy load friction in harsh marine applications. The results not only provide the comprehensively fundamental insight into the electrochemical corrosion and tribological behavior of amorphous carbon films during friction, but also bring forward the promising strategy to develop protective coatings with specialized serving demands for harsh marine applications.

CRediT authorship contribution statement

Wang Aiying: Conceptualization, Project administration, Writing – review & editing. **Ke Peiling:** Project administration, Visualization. **Guo Peng:** Conceptualization, Supervision. **Chen Rende:** Methodology. **Ma Guanshui:** Methodology. **Yang Wei:** Writing – review & editing. **Cui Li:** Formal analysis. **Li Hao:** Data curation. **Zhang Yingpeng:** Writing – original draft.

Declaration of Competing Interest

The authors declare that they have no known competing financial interests or personal relationships that could have appeared to influence the work reported in this paper.

Data availability

The raw/processed data required to reproduce these finds cannot be shared at this time as the data also forms part of an ongoing study.

Acknowledgments

This work was financially supported by the State Key Project of Fundamental Research of China (2022YFB3808802), National Science Fund for Distinguished Young Scholars of China (52025014),Natural Science Foundation of Ningbo (2022J301, 2022J305), and Director's Fund of Ningbo Institute of Materials Technology and Engineering, CAS (2022SZKY0203). The authors would like also to acknowledge Prof. Qun Wang at Hunan University for supporting the HVOF experiments.

Appendix A. Supporting information

Supplementary data associated with this article can be found in the online version at doi:10.1016/j.corsci.2023.111738.

References

[1] P. Shipway, D. McCartney, T. Sudaprasert, Sliding wear behaviour of conventional and nanostructured HVOF sprayed WC–Co coatings, Wear 259 (2005) 820–827.
[2] A. Ghabchi, T. Varis, E. Turunen, T. Suhonen, X. Liu, S.-P. Hannula, Behavior of HVOF WC-10Co4Cr coatings with different carbide size in fine and coarse particle abrasion, J. Therm. Spray. Technol. 19 (2010) 368–377.
[3] B. Kear, G. Skandan, R. Sadangi, Factors controlling decarburization in HVOF sprayed nano-WC/Co hardcoatings, Scr. Mater. 44 (2001) 1703–1707.
[4] C. Monticelli, A. Frignani, F. Zucchi, Investigation on the corrosion process of carbon steel coated by HVOF WC/Co cermets in neutral solution, Corros. Sci. 46 (2004) 1225–1237.
[5] P. Chivavibul, M. Watanabe, S. Kuroda, K. Shinoda, Effects of carbide size and Co content on the microstructure and mechanical properties of HVOF-sprayed WC–Co coatings, Surf. Coat. Technol. 202 (2007) 509–521.
[6] Q. Wang, S. Zhang, Y. Cheng, J. Xiang, X. Zhao, G. Yang, Wear and corrosion performance of WC-10Co4Cr coatings deposited by different HVOF and HVAF spraying processes, Surf. Coat. Technol. 218 (2013) 127–136.
[7] J. Cho, S. Hwang, K. Kim, Corrosion behavior of thermal sprayed WC cermet coatings having various metallic binders in strong acidic environment, Surf. Coat. Technol. 200 (2006) 2653–2662.
[8] G. Saha, T. Khan, G. Zhang, Erosion–corrosion resistance of microcrystalline and near-nanocrystalline WC–17Co high velocity oxy-fuel thermal spray coatings, Corros. Sci. 53 (2011) 2106–2114.
[9] K. Hu, X. Liu, S. Zhang, Z. Xue, Y. Yang, K. Yang, Tribocorrosion behavior of HVOF sprayed WC-based cermet coatings in sodium chloride solution environment in relation to binder phases, Surf. Coat. Technol. 435 (2022), 128248.
[10] L. Fedrizzi, L. Valentinelli, S. Rossi, S. Segna, Tribocorrosion behaviour of HVOF cermet coatings, Corros. Sci. 49 (2007) 2781–2799.
[11] P. Tang, D. He, W. Li, L. Shang, H. Zhai, L. Wang, G. Zhang, Achieving superior hot corrosion resistance by PVD/HVOF duplex design, Corros. Sci. 175 (2020), 108845.
[12] W. Chen, B. Fang, D. Zhang, X. Meng, S. Zhang, Thermal stability and mechanical properties of HVOF/PVD duplex ceramic coatings produced by HVOF and cathodic vacuum arc, Ceram. Int. 43 (2017) 7415–7423.
[13] Y. Zhao, D. He, W. Li, Q. Song, H. Zhai, B. Cheng, The role of cermet interlayer on tribological behaviors of DLC/Cr3C2–NiCr duplex coating from the perspective of carbonaceous transfer film formation, Ceram. Int. 48 (2022) 36945–36952.
[14] E. Bemporad, M. Sebastiani, D. De Felicis, F. Carassiti, R. Valle, F. Casadei, Production and characterization of duplex coatings (HVOF and PVD) on Ti–6Al–4V substrate, Thin Solid Films 515 (2006) 186–194.
[15] F. Ghadami, A.S.R. Aghdam, Improvement of high velocity oxy-fuel spray coatings by thermal post-treatments: a critical review, Thin Solid Films 678 (2019) 42–52.
[16] F. Pougoum, J. Qian, M. Laberge, L. Martinu, J. Klemberg-Sapieha, Z. Zhou, K.Y. Li, S. Savoie, R. Schulz, Investigation of Fe3Al-based PVD/HVOF duplex coatings to protect stainless steel from sliding wear against alumina, Surf. Coat. Technol. 350 (2018) 699–711.
[17] A.-Y. Wang, K.-R. Lee, J.-P. Ahn, J.H. Han, Structure and mechanical properties of W incorporated diamond-like carbon films prepared by a hybrid ion beam deposition technique, Carbon 44 (2006) 1826–1832.
[18] A. Baptista, F. Silva, J. Porteiro, J. Míguez, G. Pinto, L. Fernandes, On the physical vapour deposition (PVD): evolution of magnetron sputtering processes for industrial applications, Procedia Manuf. 17 (2018) 746–757.
[19] Y. Liu, A. Erdemir, E. Meletis, An investigation of the relationship between graphitization and frictional behavior of DLC coatings, Surf. Coat. Technol. 86 (1996) 564–568.
[20] E. Dalibón, L. Escalada, S. Simison, C. Forsich, D. Heim, S. Brühl, Mechanical and corrosion behavior of thick and soft DLC coatings, Surf. Coat. Technol. 312 (2017) 101–109.
[21] Y. Liu, H. Du, X. Zuo, P. Guo, L. Liu, K.-R. Lee, A. Wang, P. Ke, Cr/GLC multilayered coating in simulated deep-sea environment: Corrosion behavior and growth defect evolution, Corros. Sci. 188 (2021), 109528.
[22] L. Li, L.-L. Liu, X. Li, P. Guo, P. Ke, A. Wang, Enhanced tribocorrosion performance of Cr/GLC multilayered films for marine protective application, ACS Appl. Mater. Interfaces 10 (2018) 13187–13198.
[23] Y. Lifshitz, Diamond-like carbon—present status, Diam. Relat. Mater. 8 (1999) 1659–1676.
[24] T. Zhang, D. Xie, N. Huang, Y. Leng, The effect of hydrogen on the tribological behavior of diamond like carbon (DLC) coatings sliding against Al2O3 in water environment, Surf. Coat. Technol. 320 (2017) 619–623.
[25] H. Ronkainen, S. Varjus, K. Holmberg, Tribological performance of different DLC coatings in water-lubricated conditions, Wear 249 (2001) 267–271.
[26] H. Li, L. Liu, P. Guo, L. Sun, J. Wei, Y. Liu, S. Li, S. Wang, K.-R. Lee, P. Ke, Long-term tribocorrosion resistance and failure tolerance of multilayer carbon-based coatings, Friction 10 (2022) 1707–1721.

[27] Q. Wang, Y. Zhang, X. Ding, S. Wang, C.S. Ramachandran, Effect of WC grain size and abrasive type on the wear performance of HVOF-sprayed WC-20Cr3C2-7Ni coatings, Coatings 10 (2020) 660.
[28] N. Paik, Raman and XPS studies of DLC films prepared by a magnetron sputter-type negative ion source, Surf. Coat. Technol. 200 (2005) 2170–2174.
[29] C. Casiraghi, F. Piazza, A. Ferrari, D. Grambole, J. Robertson, Bonding in hydrogenated diamond-like carbon by Raman spectroscopy, Diam. Relat. Mater. 14 (2005) 1098–1102.
[30] P. Guo, R. Chen, L. Sun, X. Li, P. Ke, Q. Xue, A. Wang, Bulk-limited electrical behaviors in metal/hydrogenated diamond-like carbon/metal devices, Appl. Phys. Lett. 112 (2018), 033502.
[31] J. Robertson, Mechanical properties and coordinations of amorphous carbons, Phys. Rev. Lett. 68 (1992) 220.
[32] A. Ferrari, J. Robertson, M. Beghi, C.E. Bottani, R. Ferulano, R. Pastorelli, Elastic constants of tetrahedral amorphous carbon films by surface Brillouin scattering, Appl. Phys. Lett. 75 (1999) 1893–1895.
[33] J. Zhang, B. Zhang, Q. Xue, Z. Wang, Ultra-elastic recovery and low friction of amorphous carbon films produced by a dispersion of multilayer graphene, Diam. Relat. Mater. 23 (2012) 5–9.
[34] Y. Zhang, Q. Wang, G. Chen, C.S. Ramachandran, Mechanical, tribological and corrosion physiognomies of CNT-Al metal matrix composite (MMC) coatings deposited by cold gas dynamic spray (CGDS) process, Surf. Coat. Technol. 403 (2020), 126380.
[35] J.-P. Celis, P. Ponthiaux, F. Wenger, Tribo-corrosion of materials: interplay between chemical, electrochemical, and mechanical reactivity of surfaces, Wear 261 (2006) 939–946.
[36] W. Wang, K. Wang, Z. Zhang, J. Chen, T. Mou, F.M. Michel, H. Xin, W. Cai, Ultrahigh tribocorrosion resistance of metals enabled by nano-layering, Acta Mater. 206 (2021), 116609.
[37] J. Silva, A. Alves, A. Pinto, F. Toptan, Corrosion and tribocorrosion behavior of Ti–TiB– TiNx in-situ hybrid composite synthesized by reactive hot pressing, J. Mech. Behav. Biomed. Mater. 74 (2017) 195–203.
[38] I. Çaha, E. Erdoğan, A.M. Pinto, N. Cansever, F.L. Deepak, F. Toptan, A.C. Alves, Crystallization and additional oxide interlayers improve the tribocorrosion resistance of TiO2 nanotubular surfaces formed on Ti6Al4V, Appl. Surf. Sci. (2023), 157755.
[39] M. Daroonparvar, M.F. Khan, Y. Saadeh, C. Kay, A.K. Kasar, P. Kumar, L. Esteves, M. Misra, P. Menezes, P. Kalvala, Modification of surface hardness, wear resistance and corrosion resistance of cold spray Al coated AZ31B Mg alloy using cold spray double layered Ta/Ti coating in 3.5 wt% NaCl solution, Corros. Sci. 176 (2020), 109029.
[40] B. Hirschorn, M.E. Orazem, B. Tribollet, V. Vivier, I. Frateur, M. Musiani, Constant-phase-element behavior caused by resistivity distributions in films: I. Theory, J. Electrochem. Soc. 157 (2010) C452.
[41] B. Hirschorn, M.E. Orazem, B. Tribollet, V. Vivier, I. Frateur, M. Musiani, Determination of effective capacitance and film thickness from constant-phase-element parameters, Electrochim. Acta 55 (2010) 6218–6227.
[42] Y.-J. Lee, T.-Y. Kim, K.-R. Lee, I.-S. Yang, Humidity Dependence of the Residual Stress of Diamond-like Carbon Film, J. Korean Vac. Soc. 13 (2004) 157–163.
[43] S.J. Park, K.-R. Lee, S.-H. Ahn, J.-G. Kim, Instability of diamond-like carbon (DLC) films during sliding in aqueous environment, Diam. Relat. Mater. 17 (2008) 247–251.
[44] X.-W. Li, M.-W. Joe, A.-Y. Wang, K.-R. Lee, Stress reduction of diamond-like carbon by Si incorporation: A molecular dynamics study, Surf. Coat. Technol. 228 (2013) S190–S193.